Visualization of Fermi's Golden Rule Through Imaging of Light Emission from Atomic Silver Chains

Chi Chen, *et al.*

Science **325**, 981 (2009);
DOI: 10.1126/science.1174592

The "wavy" strategy of Fig. 4A can accommodate only a relatively modest range of applied strains (i.e., up to a few percent, for the designs reported here). A path to displays with high levels of stretchability uses non-coplanar mesh designs adapted from schemes reported for integrated circuits (*13*). Figure 4B presents optical micrographs of such a system, composed of a 16 by 16 square array of ILEDs bonded to a PDMS substrate and interconnected by electrodes supported by arc-shaped bridges, with a fraction of the pixels turned on (overall yield >80%) (see SOM and fig. S15 for details). The shapes of these bridges change in response to deformations of the display, in a way that isolates the ILEDs from any significant strains (figs. S16 and S17). In particular, calculation shows that for strains of 24%, as defined by the change in separation between inner edges of adjacent device islands, the maximum strains in the ILED and quantum well are only 0.17 and 0.026%, respectively. The computed change in emission wavelength is less than ~0.3 nm (see SOM for details). Figure 4C provides optical micrographs of four pixels in this display, in their off and on states, with (top) and without (bottom) external illumination, respectively, in compressed and stretched configurations. The images show the expected reduction in the heights of the arc-shaped bridges that lie in the direction of the applied tensile force (i.e., along the interconnects that run from lower left to upper right), together with an increase in the heights of the bridges in the orthogonal direction, due to the Poisson effect. This mechanical response is fully elastic—the bending-induced strains in the interconnects are small, the strains in the ILEDs are negligible, and the strain in the PDMS is well within its linear response regime. The data in Fig. 4, D and E, are consistent with this mechanics, as are the associated mechanics calculations. In particular, the current-voltage characteristics of a typical device do not change in a measurable way for applied strains up to ~22%, and we observe no degradation on cycling up to a few hundred times (500 times). Recent work demonstrates the use of smaller collections of large, conventional ILEDs in deformable devices that use different designs (*24*, *25*).

The schemes reported here for creating thin, small inorganic LEDs and for integrating them into display and lighting devices create design options that are unavailable with conventional procedures. The planar processing approaches for interconnect resemble those that are now used for organic devices and, for example, large-area electronics for liquid crystal displays, thereby conferring onto inorganic LED technologies many of the associated practical advantages. In large-area, high–pixel count systems (e.g., 1 million pixels per square meter), the ability to use LEDs with sizes much smaller than those of the individual pixels is critically important to achieve efficient utilization of the epitaxial semiconductor material, for reasonable cost. The minimum sizes of devices reported here are limited only by the resolution and registration associated with manual tools for photolithography.

References and Notes

1. S.-C. Lo, P. L. Burn, *Chem. Rev.* **107**, 1097 (2007).
2. F. So, J. Kido, P. Burrows, *MRS Bull.* **33**, 663 (2008).
3. D. A. Gaul, W. S. Rees Jr., *Adv. Mater.* **12**, 935 (2000).
4. S. Nakamura, G. Fasol, *The Blue Laser Diode: GaN Based Light Emitters and Lasers* (Springer, New York, 1997).
5. E. Yablonovitch, D. M. Hwang, T. J. Gmitter, L. T. Florez, J. P. Harbison, *Appl. Phys. Lett.* **56**, 2419 (1990).
6. H. X. Jiang, S. X. Jin, J. Li, J. Shakya, J. Y. Lin, *Appl. Phys. Lett.* **78**, 1303 (2001).
7. M. Konagai, M. Sugimoto, K. Takahashi, *J. Cryst. Growth* **45**, 277 (1978).
8. E. Yablonovitch, T. Gmitter, J. P. Harbison, R. Bhat, *Appl. Phys. Lett.* **51**, 2222 (1987).
9. C. Camperi-Ginestet, M. Hargis, N. Jokerst, M. Allen, *IEEE Trans. Photon. Tech. Lett.* **3**, 1123 (1991).
10. C. Carter-Coman, R. Bicknell-Tassius, A. S. Brown, N. M. Jokerst, *Appl. Phys. Lett.* **70**, 1754 (1997).
11. M. A. Meitl *et al.*, *Nat. Mater.* **5**, 33 (2006).
12. D. Y. Khang, H. Jiang, Y. Huang, J. A. Rogers, *Science* **311**, 208 (2006).
13. D.-H. Kim *et al.*, *Proc. Natl. Acad. Sci. U.S.A.* **105**, 18675 (2008).
14. J. Yoon *et al.*, *Nat. Mater.* **7**, 907 (2008).
15. M. Tamura *et al.*, *Jpn. J. Appl. Phys.* **37**, 3576 (1998).
16. E. F. Schubert, *Light-Emitting Diodes* P. 43, (Cambridge Univ. Press, Cambridge, UK, 2003).
17. C. L. Chen *et al.*, *Appl. Phys. Lett.* **48**, 535 (1986).
18. G. Stareev, *Appl. Phys. Lett.* **62**, 2801 (1993).
19. D. P. Bour *et al.*, *IEEE J. Quantum Electron.* **30**, 593 (1994).
20. F. H. Pollak, *Surf. Sci.* **37**, 863 (1973).
21. M. Chandrasekhar, F. H. Pollak, *Phys. Rev. B* **15**, 2127 (1977).
22. S. H. Pan *et al.*, *Phys. Rev. B* **38**, 3375 (1988).
23. H. Jiang *et al.*, *Proc. Natl. Acad. Sci. U.S.A.* **104**, 15607 (2007).
24. D. S. Gray, J. Tien, C. S. Chen, *Adv. Mater.* **16**, 393 (2004).
25. F. Axisa, F. Bossuyt, T. Vervust, J. Vanfleteren, *2nd Electronics System-integration Technology Conference (ESTC 2008)*, 1387, Greenwich, UK, 1 to 4 September 2008.

26. We thank T. Banks for help with processing using facilities at the Frederick Seitz Materials Research Laboratory; S. Mikael, V. Malyarchuk, H. C. Ko, and S.-G. Koo for assistance with display operating interface; J. D. Sulkin for help with current-voltage-emission measurement; A. P. Le for help with measurement of emission spectra; and C. Conway, Z. Johnson, and H.-S. Kim for help with photography. This material is based on work supported by Ford Motor Company, the NSF (grant DMI-0328162), and the U.S. Department of Energy, Division of Materials Sciences (Award No. DE-FG02-07ER46471), through the Materials Research Laboratory and Center for Microanalysis of Materials (DE-FG02-07ER46453) at the University of Illinois at Urbana-Champaign. S.-I. Park and R.-H. Kim thank Samsung for doctoral fellowships.

Supporting Online Material

www.sciencemag.org/cgi/content/full/325/5943/977/DC1
Materials and Methods
Figs. S1 to S19
References

1 May 2009; accepted 1 July 2009
10.1126/science.1175690

Visualization of Fermi's Golden Rule Through Imaging of Light Emission from Atomic Silver Chains

Chi Chen,[1] C. A. Bobisch,[2] W. Ho[1,2]*

Atomic-scale spatial imaging of one-dimensional chains of silver atoms allows Fermi's golden rule, a fundamental principle governing optical transitions, to be visualized. We used a scanning tunneling microscope (STM) to assemble a silver atom chain on a nickel-aluminum alloy surface. Photon emission was induced with electrons from the tip of the STM. The emission was spatially resolved with subnanometer resolution by changing the tip position along the chain. The number and positions of the emission maxima in the photon images match those of the nodes in the differential conductance images of particle-in-a-box states. This surprising correlation between the emission maxima and nodes in the density of states is a manifestation of Fermi's golden rule in real space for radiative transitions and provides an understanding of the mechanism of STM-induced light emission.

The scanning tunneling microscope (STM), which is based on the tunneling effect, has been used to visualize various quantum phenomena in real space, including the quantum corral (*1*), quantum mirage (*2*), and particle-in-a-box states (*3*, *4*). All of these demonstrations involved the localization of the electron density of states in confined nanostructures. Light emission from the STM junction reveals a different kind of quantum phenomenon that involves the optical transitions and inelastic electron tunneling (IET) processes in single molecules (*5*, *6*) and nanostructures (*7*). Furthermore, photon intensity imaging with atomic resolution has been demonstrated (*8*–*10*). The spatial resolution in these optical experiments originates from the precision of the STM in injecting electrons in a confined space, although the emitted photons are collected in the far field. This atomic-scale optical detection can reveal aspects of the molecules and nanostructures that are hidden when probed with other techniques.

Imaging of STM light emission has not yet been directly correlated with the underlying elec-

[1]Department of Chemistry, University of California, Irvine, CA 92697, USA. [2]Department of Physics and Astronomy, University of California, Irvine, CA 92697, USA.

*To whom correspondence should be addressed. E-mail: wilsonho@uci.edu

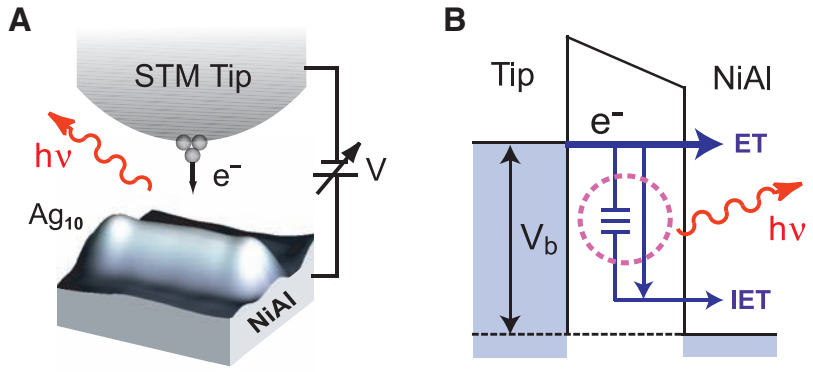

Fig. 1. (**A**) Illustration of Ag_{10} chain in the tunnel junction, assembled on the NiAl(110) substrate. The Ag_{10} topography shown in the figure was taken at a bias of 2.8 V and tunneling current of 1 nA. (**B**) Schematic representation of photon emissions from two coupled IET processes, involving an electronic transition in resonance with the excitation of plasmon modes in the junction. The radiative decay of plasmons is detected as photons in the far field. In the resonant coupling, the plasmons oscillate at the same frequency as the light emitted in the transition between two electronic states of the Ag_{10} chain.

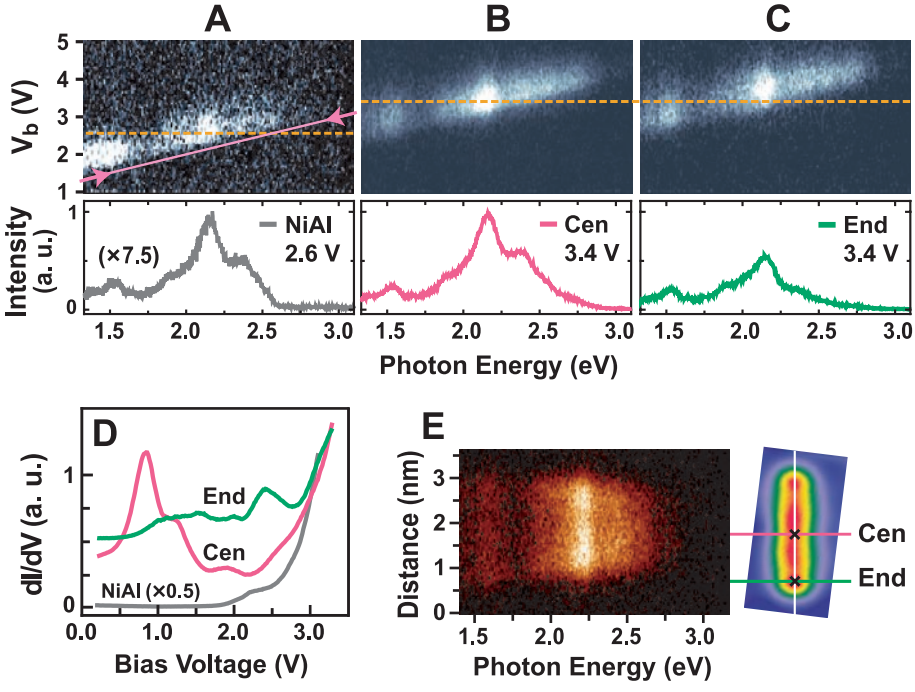

Fig. 2. (**A** to **C**) Excitation mappings and spectra taken over the NiAl substrate (A), the center (Cen) (B), and end (End) (C) of Ag_{10}, as indicated in the right panel of (E). (Upper panels) Excitation mappings are composed of a series of spectra taken with bias voltages from 1.0 to 5.0 V at 0.05-V intervals. The horizontal dashed lines (orange) represent the bias voltage for the bottom spectra. The quantum cutoff for substrate emission is shown as the solid line (magenta) in (A). (Lower panels) Spectra at the center [red (B)] and end [green (C)] of Ag_{10} at 3.4-V sample bias compared to the spectrum of the NiAl substrate [gray (A)] at 2.6 V. All spectra were accumulated for 20 s. (**D**) *dI/dV* spectra recorded at the center and end of the chain and over the NiAl substrate. At lower bias voltages (V_b < 2.8 V), the measured LDOS are mostly dominated by the Ag_{10}. At higher biases, the signal from the NiAl substrate surpasses that of Ag_{10}. (**E**) (Left) Emission intensity map composed of 96 spectra (1-s accumulation time each) taken along the center line of Ag_{10} chain (white line). (Right) Topographical image of Ag_{10} chain (7° rotation from vertical). The image size is 1.8 nm × 3.6 nm. Both panels in (E) were recorded at 3.4 V and 6 nA. The positions for spectra taken over the chain (Cen, End) are indicated on the topographic image. The position for spectra taken over the NiAl substrate is outside the range of this image. All spectra shown here and used for photon images are raw data from the spectrometer without grating efficiency correction.

tronic structure of the adsorbate. The connection between the photon yield and the density of states remains to be further clarified. Even though the IET mechanism was proposed by Nazin *et al.* (*7*), the mechanisms of these radiative transitions and the fundamental selection rules have not been well understood. Here, we describe a system in which the interaction between the initial and final states that give rise to well-defined light emission arises via coupling through the momentum operator.

Here, we report photon imaging of optical transitions from atomic Ag chains to reveal the underlying physical principles and a direct visualization of Fermi's golden rule in real space (*11*). We manipulated Ag atoms on a NiAl(110) substrate into one-dimensional (1D) chains following the method described in (*3*). An atomic chain serves as a model system to realize particle-in-a-box electronic states both in energy and in space. These electronic states could be visualized as a series of differential conductance (*dI/dV*) images that have different numbers of nodes and antinodes (*4*). This spatial distribution of local density of states (LDOS) dominates the probabilities of radiative electronic transitions in the spatial imaging of the emitted light. The experimental visualization of Fermi's golden rule serves to elucidate one of the fundamental principles in quantum mechanics.

Single Ag atoms were produced by field emission of the Ag tip on a clean NiAl surface and were characterized by *dI/dV* spectroscopy (*7*). Every Ag atom exhibits a single peak at 2.1 to 2.2 V in the *dI/dV* spectrum, which can be easily distinguished from other atoms (Ni or Al) on the surface. After the addition of each Ag atom to the chain, *dI/dV* spectra along the chain were recorded to characterize the electronic states at each chain length. Results are presented here for the representative case of Ag_{10}, which is the longest chain that was built in this experiment (Fig. 1A).

Photon emission from the STM junction occurs through radiative decay of localized surface plasmons that are excited by IET processes (*5*, *12*, *13*). These junction plasmons decay as broadband emission with multiple peaks. Their spectral shape is primarily determined by the structure of the STM tip apex at the nanometer scale and also by the dielectric properties of both the tip and substrate (*14*). A schematic illustration of radiative emission in the tunneling process is shown in Fig. 1B.

When electrons tunnel through the junction, both elastic tunneling (ET) and IET are possible. The IET channel can be observed when it couples to the excitation of other physical quantities such as molecular vibrations, substrate phonons, plasmons, or electronic transitions. For example, if the IET couples to a vibrational mode, it can be measured through a change in the conductance (*dI/dV*) as the voltage across the tunneling gap passes through the value V_ω corresponding to the vibrational energy $eV_\omega = \hbar\omega$,

where e is the charge of an electron, $\hbar$ is Planck's constant divided by 2π, and ω is angular frequency (*15*).

In our experimental case, the IET process could be observed because of the coupling with plasmon modes and electronic transitions. Unlike the ET process, which probes the LDOS only at the applied bias voltage, the IET channel involves both the initial and final LDOS of the inelastic process. The IET efficiency is determined by two factors: The first factor involves the radiative transition between the initial and final states in the tunneling process, and the second factor is that the coupling to the plasmon modes in the junction leads to field enhancement of the radiation field. However, no direct experimental evidence could test this IET process, especially when its analysis required the interpretation of local variations in photon intensity imaging (*16*).

The radiative emission of plasmons can be characterized by "excitation mapping" (Fig. 2, A to C, upper panels), which reveals the spectral structures of the plasmon emission that shift with the bias voltage. From the spectral evolution of the substrate with increasing bias (Fig. 2A, upper panel), two main emission bands were resolved from the tip–NiAl junction; one was in the visible spectrum and the other lies in the near-infrared. The highest photon energy detected was 2.95 eV, even with higher biases. This is strong evidence for the plasmon emission mechanism. If the emission is through different mechanisms (i.e., hot electron and hole recombination), then higher-energy photons should be emitted as the bias is increased.

When the Ag_{10} chain was in the junction, the emission spectral features of the tip–Ag_{10}–NiAl junction remained similar to that of tip–NiAl junction; no additional mode was observed (Fig. 2, B and C, bottom panels). This observation is distinct from theoretical predictions of localized plasmon modes of free atomic chains (*17*). Because the length of Ag_{10} from the topographic image is 3.2 to 3.4 nm, depending on the bias, it may be too confined to support localized plasmon modes (*18*).

Although no new plasmon mode was found, the spectral shape and intensity were affected by the presence of the Ag_{10} chain. First, the overall intensity was enhanced with Ag_{10} in the junction (~7.5 times stronger at the center) as compared with bare NiAl (comparing Fig. 2B to 2A). Second, the relative intensity of the visible band was enhanced over the near-infrared band, comparing the upper panels of Fig. 2B and 2C with Fig. 2A, especially the mode at $h\nu = 2.2$ eV, where h is Planck's constant and ν is frequency. The introduction of Ag_{10} in the junction changed the final state of inelastic electron tunneling from that around the Fermi level of NiAl to states of the Ag_{10} chain. Thus, the bias for IET excitation of the same plasmon modes was up-shifted by about 0.8 V at the center and by 1.1 V toward the end of the chain (Fig. 2, B and C, upper panels), compared to NiAl (Fig. 2A, upper panels). This up-shift in the excitation bias and the invariance of the plasmon modes have also been observed for light emissions from molecular adsorbate on the metal surface (*7*, *19*).

An additional ~0.3 V is required to excite the same plasmon modes at the end as compared to the center of the Ag_{10} chain. This up-shift in excitation energy has its origin in the dI/dV spectra shown in Fig. 2D, where lower-energy states dominate in the central part of Ag_{10}, whereas higher-energy states populate preferentially toward the ends of the chain. This variation of LDOS of Ag_{10} also occurs in atomic Au and Pd chains (*3*, *4*, *20*), leading to a difference in their spectral intensity at the same bias. For example, as shown in the bottom panels of Fig. 2, B and C, the overall intensity around $h\nu = 2.4$ eV is higher at the center than at the ends for a bias of 3.4 V. If the dashed line in Fig. 2C is shifted up by 0.3 V, then the spectrum becomes similar to that of 3.4 V at the center. Qualitatively, the shift of the excitation bias with chain position follows the same trend as the shift in dI/dV (*7*). However, the quantitative relation of these two shifts is complex, because the electronic states at the ends of the chain involve a dramatic transition from Ag_{10} to NiAl.

Clear contrasts in emission intensities along Ag_{10} were obtained by plotting a series of spectra for different positions along the chain to yield a 2D intensity contour (Fig. 2E, left panel). Comparison with the corresponding topography (Fig. 2E, right panel) shows that the photon emission is confined within the chain. For lower photon energies ($h\nu < 1.7$ eV), the emission is distributed throughout the chain. For higher photon energies, the emission intensity is seen to spatially narrow toward the center. In addition, the distribution along Ag_{10} is not uniform in intensity and contains emission maxima and minima. Roughly, the number of maxima decreases from three or four to one as photon energy increases. The observed emission pattern and change in the number of maxima suggest a close connection between the optical transition and the particle-in-a-box properties of Ag_{10}.

This connection between dI/dV and photon images is revealed in Fig. 3 for decreasing photon energies. The oscillating electron densities for the different final states, $dI/dV_{(f)}$, are shown horizontally in Fig. 3D. The number of maxima and minima (nodes) in the $dI/dV_{(f)}$ images

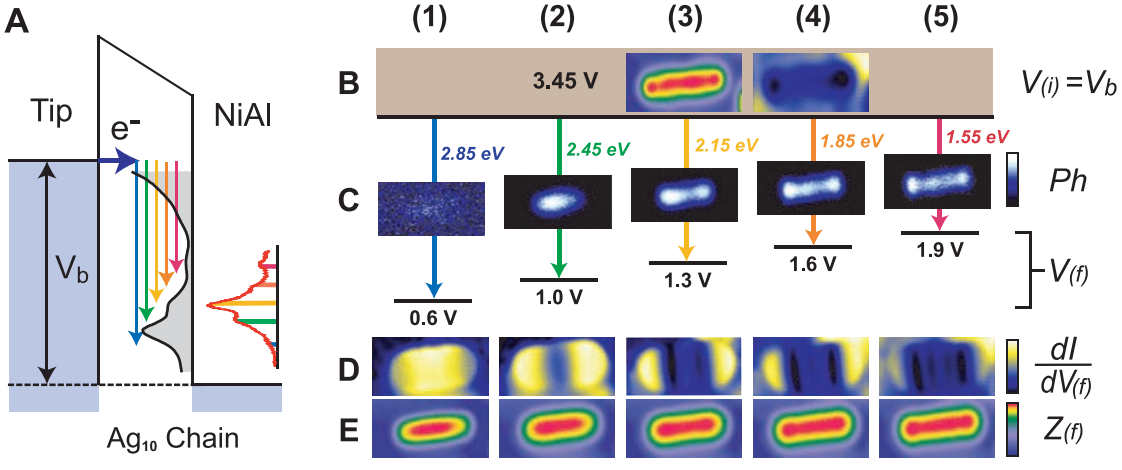

Fig. 3. (**A**) Schematic representation of radiative transitions in Ag_{10}. Electrons undergo transitions between the Ag chain states (black curve, dI/dV at center of Ag_{10}), and the corresponding photon emission spectrum is shown (red curve, emission at the center of Ag_{10}). The horizontal arrow indicates the injection of a tunneling electron. Five vertical arrows of different colors show transitions into the LDOS of Ag_{10}. (**B**) Topography (left) and simultaneous dI/dV image (right) at 3.45 V, which is the initial state of all the transitions shown below. (**C**) Photon emission (Ph) for different energies from transitions between the same initial state $V_{(i)}$ to five different final states at $V_{(f)}$. The photon images shown here are 3.6 nm × 1.8 nm (96 × 48 pixels) and accumulated under 6-nA tunneling current and 1-s spectral accumulation at each pixel. The range for the integrated intensity is ±0.2 eV. (As an example, we integrated the spectrum at each pixel from 1.28 to 1.32 eV for the photon image at 1.3 eV.) The photon images show zero, one, two, three, and four maxima as the photon energy decreases from 2.85 to 1.55 eV. Each photon image is displayed over the full range of intensity for the shown palette, so the intensities cannot be compared from one to another. (**D**) $dI/dV_{(f)}$ images for the five final states showing zero, one, two, three, and four nodes (dark bands) for the ground state and first, second, third, and fourth excited states of the particle in a box. The positions of the emission maxima coincide with the nodes in $dI/dV_{(f)}$ images. (**E**) Topographic images [$Z_{(f)}$] of the Ag_{10} chain at biases corresponding to different final states $V_{(f)}$. The images of this chain yield a length of 2.9 to 3.4 nm, with the variation due to the dependence of the image on bias voltage. Images for (B), (D), and (E) have the same size: 3.9 nm × 1.95 nm (64 × 32 pixels), taken at 1-nA tunneling current.

increases with the energy of the states [$eV_{(f)}$]. The ends of Ag_{10} appear as two bright lobes due to the enhancement of edge effects during *dI/dV* imaging (*4*). As the bias $V_{(f)}$ increases, sequential $dI/dV_{(f)}$ images could be predominantly assigned to the ground, first, second, third, and fourth excited states (Ψ_1, Ψ_2, Ψ_3, Ψ_4, and Ψ_5, respectively) of this 1D particle-in-a-box system. At each chosen bias voltage, the density does not correspond to a pure state and is a weighted sum of nearby states (*3*). The voltages are chosen to reveal the dominance of one state exhibiting zero, one, two, three, or four nodes in $dI/dV_{(f)}$. As expected, separations between the nodes become smaller for higher-energy states. When the bias voltage is higher than 2.8 V, *dI/dV* is dominated by the NiAl states (Fig. 2D), and its fine structures are smeared out. For example, at 3.45 V (Fig. 3B), the profile of Ag_{10} is still discernible, but oscillating patterns can no longer be identified.

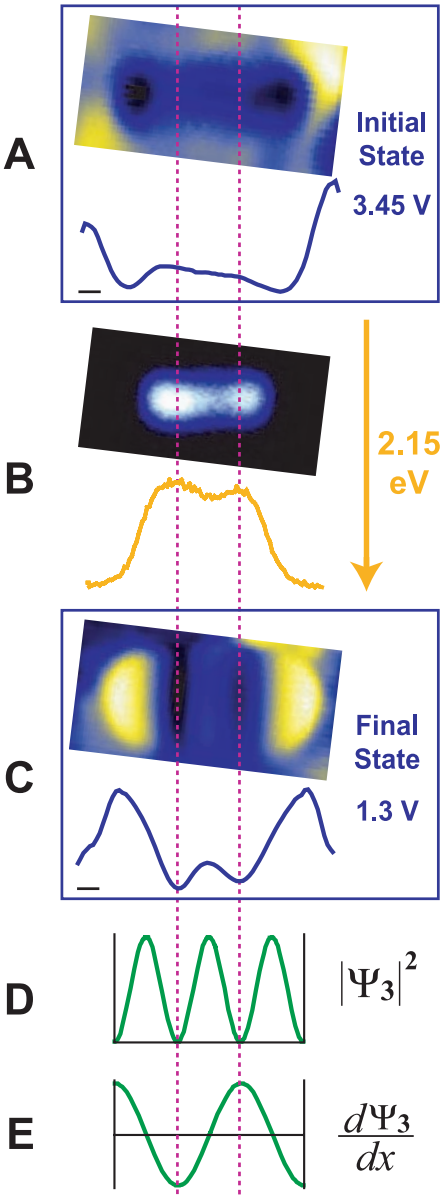

Fig. 4. (**A** and **C**) *dI/dV* images and cross-sectional line cuts of the initial state (3.45 V) and final state (1.3 V). (**B**) Photon image and its cross-sectional line cut at $h\nu$ = 2.15 eV. (**D** and **E**) All images and cross-sectional line cuts are aligned (the two vertical dashed lines) with the electron density (D) and derivative (E) of Ψ_3, the wave function for the second excited state of the 1D particle in a box with infinite walls.

The role of the spatially oscillating electronic states of Ag_{10} in the optical transitions is determined from imaging of the photon emission. Photon imaging of different emission energies at a fixed bias of 3.45 V allows the investigation of final-state effects and is shown schematically in Fig. 3A. Not every final state could be probed, because of the limited photon detection window of the charge-coupled device (1.3 to 3.0 eV) and spectral range of the plasmon modes. For 3.45-V bias, final states from Ψ_1 to Ψ_5 can be accessed. With emission energies from 2.85 to 1.55 V, photon images show zero (nearly no signal), one, two, three, and four bright maxima (Fig. 3C). A comparison with the corresponding final-state $dI/dV_{(f)}$ images (Fig. 3D) reveals that the number of emission maxima is equivalent to the number of nodes. Furthermore, the distributions of emission maxima directly coincide with the positions of nodes in $dI/dV_{(f)}$ images. The entire emission spectrum was recorded at each pixel of the *x*-*y* image. The different images in Fig. 3C correspond to integrated energy slices within each spectrum. These results are consistent for different chain lengths, scanning directions, and biases. We can completely exclude any influence on the photon emission images from feedback or tip movement (*7*, *8*).

The probability of tunneling (both ET and IET) depends on the magnitude of the LDOS. The photon images should reflect the LDOS of the initial state (Fig. 3B) and the final state (Fig. 3D). However, the observed maxima in the photon images do not match the spatial distribution of high LDOS in the initial- or final-state *dI/dV* images.

To explain this mismatch, the tunneling process needs to be integrated with the optical transition. The rate of transition w_{if} between two states $|i\rangle$ and $|f\rangle$ from Fermi's golden rule (*21*) is given by

$$w_{if} = \frac{2\pi}{\hbar}|U_{if}|^2\ \delta(E_f - E_i \pm \hbar\omega) \quad (1)$$

$$U_{if} = \frac{eA_0}{2mc}\boldsymbol{\varepsilon}\cdot\langle i|\mathbf{p}|f\rangle \quad (2)$$

where E_i and E_f are the energy of the initial and final states $|i\rangle$ and $|f\rangle$, respectively, and ω is the angular frequency of the emitted light. The matrix element U_{if} represents the radiative transition between the two states, in which $A_0\boldsymbol{\varepsilon} = \mathbf{A}$ is the vector potential. The spatial dependence of the matrix element is given by

$$u_{if}(\vec{r}) \propto \Psi_i(\vec{r})\,\hat{\mathbf{p}}\,\Psi_f(\vec{r}) \quad (3)$$

The Ag_{10} eigenstates are well described by the 1D particle-in-a-box wave functions. The momentum operator can be replaced by the position representation

$$u_{if}(x) \propto \Psi_i(x)\frac{d}{dx}\Psi_f(x) \quad (4)$$

From this equation, it is seen that the maximum emission occurs at positions where the derivative of the wave function is maximum (that is, momentum is largest).

The high-energy initial state $\Psi_i(x)$ can be considered as having weak spatial variations in the interior of the chain, because the higher particle-in-a-box states mix with the high density of smoothly varying substrate states (Fig. 2D). Thus, the symmetry of emission pattern is determined by $\frac{d\Psi_f(x)}{dx}$; that is, the derivative of the final state in the range of energies where the density of substrate states is low. In the case of Ag_{10}, we observe maxima of emission at nodes of the *dI/dV* images (Fig. 3). For example, in Fig. 4, the cross-sectional line cuts of the initial state (3.45 V), photon intensity at $h\nu$ = 2.15 eV, and the final state (1.3 V) are aligned with the electron density $|\Psi_3|^2$ and derivative of the wave function $\frac{d\Psi_3}{dx}$ of the ideal Ψ_3. The final state at 1.3 V shows two nodes correspond to minima in $|\Psi_3|^2$ and extrema in $\frac{d\Psi_3}{dx}$ (Fig. 4, D and E). There are, in total, four extrema in $\frac{d\Psi_3}{dx}$: two at the nodes and two at the ends. However, photon emission is observed only at the nodes. These results are consistent with Fermi's golden rule, because the matrix element contains not only the derivative of the final state $\frac{d\Psi_3}{dx}$ but also the overlap with the initial state $\Psi_i(x)$. The LDOS for the initial state $\Psi_i(x)$ vanish at the ends for a particle in a box with infinite walls and are nearly zero for the Ag_{10} chain (Fig. 4A). The rapid rise in LDOS outside the chain in Fig. 4A is associated with the NiAl substrate states (Fig. 2D). At high bias values, the Ag_{10} states no longer maintain their distinct particle-in-a-box characters because of strong mixing with the NiAl states.

The Ag_{10} chain is adsorbed on the metallic NiAl(110) substrate. Along the [110] direction, NiAl has a band gap that is responsible for the low differential conductance (*dI/dV*) up to ~2.0 V bias voltage (Fig. 2D) (*22*). The troughs on the surface provide a template for constructing the 1D Ag chains. Because of the band gap, the particle-in-a-box states are weakly coupled to the substrate states and remain distinct for states below ~ 2.0 V. The radiative process is shown schematically in Fig. 1B, where the intensity of the detected light is enhanced, arising from the coupling of the electronic transition for the plasmon modes in the junction. When the coupling is in resonance, light detected in the far field is enhanced. Such a plasmon-enhanced field is quite general and is determined at the atomic scale in the present experiment. Thus, the use of a Ag tip is preferred over other tips such as W that have strongly damped plasmons. The plasmon modes are revealed by the spectra in the bottom panels of Fig. 2, A to C. The intensity of the radiative plasmon decay does not exhibit spatial variations away from surface inhomogeneities.

The observed spatial and spectral variations in the photon imaging of the Ag chain (Figs. 3C and 4B) are dominated by the LDOS of the Ag_{10} chain, as described by Eq. 4, and coupling to the plasmons serves to strengthen the emitted light intensity. Because of the relative spatial uniformity of the initial state, the emitted light intensity is highlighted by the gradient of the final state, $\frac{d\Psi_f}{dx}$. In (*7*), the data led to the conclusion that light emission is caused by the coupling of the initial state $|i\rangle$ and final state $|f\rangle$ via the IET process, $\langle i|\mathbf{V}|f\rangle$, where $\mathbf{V}$ is the interaction potential. In our experiment, it is refined by Fermi's golden rule, in which $|i\rangle$ and $|f\rangle$ are connected by the momentum operator $\mathbf{p}$, as $\langle i|\mathbf{p}|f\rangle$. This refinement and the association of $\mathbf{V}$ with $\mathbf{p}$ are not revealed by spectroscopy at discrete points as in (*7*). The transition still goes through the same initial and final states, but the momentum operator in the matrix element gives rise to the seemingly surprising spatial images.

Although only results from Ag_{10} are presented here, the correspondence between nodes and emission maxima was also observed for Ag_2 through Ag_9. The wave functions for the particle-in-a-box–like atomic chains are simple and exhibit distinct features in energy and space, most notably the nodal structures. By varying the bias voltage to control tunneling electrons and the radiative transition in inelastic tunneling, the STM is used to obtain spatially and spectrally resolved photon images that lead to direct visualization of Fermi's golden rule, one of the fundamental principles in quantum mechanics. In addition, these results reveal the basic mechanisms underlying optical phenomena at the nanoscale, where light fields with wavelengths much greater than the dimension of the radiator are enhanced by coupling to plasmons.

References and Notes

1. M. F. Crommie, C. P. Lutz, D. M. Eigler, *Nature* **363**, 524 (1993).
2. H. C. Manoharan, C. P. Lutz, D. M. Eigler, *Nature* **403**, 512 (2000).
3. N. Nilius, T. M. Wallis, W. Ho, *Science* **297**, 1853 (2002).
4. T. M. Wallis, N. Nilius, W. Ho, *Phys. Rev. Lett.* **89**, 236802 (2002).
5. X. H. Qiu, G. V. Nazin, W. Ho, *Science* **299**, 542 (2003).
6. S. W. Wu, G. V. Nazin, W. Ho, *Phys. Rev. B* **77**, 205430 (2008).
7. G. V. Nazin, X. H. Qiu, W. Ho, *Phys. Rev. Lett.* **90**, 216110 (2003).
8. R. Berndt *et al.*, *Phys. Rev. Lett.* **74**, 102 (1995).
9. R. Berndt *et al.*, *Science* **262**, 1425 (1993).
10. G. Schull, M. Becker, R. Berndt, *Phys. Rev. Lett.* **101**, 136801 (2008).
11. The details of this experiment are available as supporting material on *Science* Online.
12. R. Berndt, J. K. Gimzewski, P. Johansson, *Phys. Rev. Lett.* **67**, 3796 (1991).
13. P. Johansson, R. Monreal, P. Apell, *Phys. Rev. B* **42**, 9210 (1990).
14. K. Meguro, K. Sakamoto, R. Arafune, M. Satoh, S. Ushioda, *Phys. Rev. B* **65**, 165405 (2002).
15. B. C. Stipe, M. A. Rezaei, W. Ho, *Science* **280**, 1732 (1998).
16. R. Berndt, J. K. Gimzewski, *Phys. Rev. B* **48**, 4746 (1993).
17. J. Yan, Z. Yuan, S. Gao, *Phys. Rev. Lett.* **98**, 216602 (2007).
18. S. A. Maier, H. A. Atwater, *J. Appl. Phys.* **98**, 011101 (2005).
19. G. Hoffmann, L. Libioulle, R. Berndt, *Phys. Rev. B* **65**, 212107 (2002).
20. N. Nilius, T. M. Wallis, W. Ho, *J. Phys. Chem.* **109**, 20657 (2005).
21. G. C. Schatz, M. A. Ratner, *Quantum Mechanics in Chemistry* (Dover, New York, 2002), chap. 4 and 5.
22. S. C. Lui, M. H. Kang, E. J. Mele, E. W. Plummer, D. M. Zehner, *Phys. Rev. B* **39**, 13149 (1989).

23. Supported by the Chemical Science, Geo- and Bioscience Division, Office of Science, U. S. Department of Energy, under grant DE-FG02-04ER1595, and by the Alexander von Humboldt Foundation through a Feodor Lynen Fellowship to C.A.B. We thank R. Wu, D. L. Mills, P. Chu, Y. Jiang, and N. Ogawa for inspiring discussions.

Supporting Online Material

www.sciencemag.org/cgi/content/full/325/5943/981/DC1
Materials and Methods
Fig. S1

6 April 2009; accepted 26 June 2009
10.1126/science.1174592

Homogeneous Distribution of ^{26}Al in the Solar System from the Mg Isotopic Composition of Chondrules

Johan Villeneuve,[1]* Marc Chaussidon,[1] Guy Libourel[1,2]

The timing of the formation of the first solids in the solar system remains poorly constrained. Micrometer-scale, high-precision magnesium (Mg) isotopic analyses demonstrate that Earth, refractory inclusions, and chondrules from primitive meteorites formed from a reservoir in which short-lived aluminum-26 (^{26}Al) and Mg isotopes were homogeneously distributed at ±10%. This level of homogeneity validates the use of ^{26}Al as a precise chronometer for early solar system events. High-precision chondrule ^{26}Al isochrons show that several distinct chondrule melting events took place from ~1.2 million years (My) to ~4 My after the first solids condensed from the solar nebula, with peaks between ~1.5 and ~3 My, and that chondrule precursors formed as early as $0.87^{+0.19}_{-0.16}$ My after.

Models of the evolution of the early solar system rely on knowledge of the precise time scales for the physical and chemical processes that occurred in the early accretion disk and led to the formation of calcium-aluminum–rich inclusions (CAIs) and chondrules, which are the building blocks of primitive meteorites (chondrites). Short-lived ^{26}Al [half-life ($T_{1/2}$) = 0.73 million years (My)] is possibly the most accurate chronometer for the first few million years of solar system history, provided that it was homogeneously distributed in the disk. Previous studies of various meteoritic components showed that ^{26}Al was widespread in the disk, but its level of homogeneity has never been quantified precisely. From numerous mineral ^{26}Al isochrons in CAIs, a canonical value of ~5×10^{-5} was inferred for the initial ^{26}Al/^{27}Al ratio [hereafter $(^{26}Al/^{27}Al)_0$] when CAIs crystallized (*1*). This value is slightly lower than 5.23 (±0.13) × 10^{-5}, which was determined from the bulk ^{26}Al isochron of Allende CAIs (*2*) [used in our work instead of 5.85 (±0.05) × 10^{-5} (*3*)], which indicates that the crystallization of CAIs followed closely after (50,000 years at most) the condensation of their precursors. The bulk ^{26}Al isochron precisely defines an initial Mg isotopic composition ($\delta^{26}Mg^*_0$) for CAI precursors of −0.040 ± 0.029 per mil (‰) (*2*). If ^{26}Al and Mg isotopes were homogeneously distributed in the inner solar system, then CAIs $\delta^{26}Mg^*_0$ can be taken as the initial Mg isotopic composition of the solar system when ^{26}Al/^{27}Al was 5.23 (±0.13) × 10^{-5}. Any object that formed later (when $^{26}Al/^{27}Al < 5.23 \times 10^{-5}$) must be characterized by a more radiogenic $\delta^{26}Mg^*_0$ value. The increase of $\delta^{26}Mg^*_0$ is a function of the Al/Mg ratio of the reservoir in which the object, or its precursors, resided before the last melting event. Al-rich and ferromagnesian chondrules from unequilibrated ordinary chondrites (UOCs) and carbonaceous chondrites (CCs) show mineral ^{26}Al isochrons with $(^{26}Al/^{27}Al)_0 < 2 \times 10^{-5}$ (*4*–*12*); that is, much lower than that of CAIs. Because the $\delta^{26}Mg^*_0$ of chondrules has never been precisely determined, the data from chondrules cannot be compared to those of CAIs nor to the theoretical Mg isotope growth curve calculated for the solar nebula for a homogeneous distribution of ^{26}Al and Mg isotopes.

We developed high-precision analysis of Al and Mg isotopes using the Centre de Recherches Petrographiques et Geochimiques (CRPG)–CNRS Cameca ion microprobe (ims 1270) to determine precisely (even for low Al/Mg ratios)

[1]Centre de Recherches Petrographiques et Geochimiques (CRPG)–Nancy Université–CNRS, UPR 2300, 15 Rue Notre-Dame des Pauvres, Boite Postale 20, 54501 Vandoeuvre-lès-Nancy, France. [2]Ecole Nationale Supérieure de Géologie (ENSG)–Nancy Université, Rue du Doyen Marcel Roubault, Boite Postale 40, 54501 Vandoeuvre-lès-Nancy, France.

*To whom correspondence should be addressed. E-mail: johanv@crpg.cnrs-nancy.fr